



Realizing efficient oxygen evolution at low overpotential via dopant-induced interfacial coupling enhancement effect

Wei Luo^{a,b}, Yanli Yu^a, Yucheng Wu^a, Zemian Ma^a, Xueying Ma^a, Yimin Jiang^a, Wei Shen^a, Rongxing He^{a,*}, Wei Su^{b,*}, Ming Li^{a,*}

^a Key Laboratory of Luminescence Analysis and Molecular Sensing (Southwest University), Ministry of Education, College of Chemistry and Chemical Engineering, Southwest University, Chongqing 400715, PR China

^b Guangxi Key Laboratory of Natural Polymer Chemistry and Physics, Guangxi Teachers Education University, Nanning 530001, PR China

ARTICLE INFO

Keywords:

Fe-CoN/CoS₂
Interfacial coupling enhancement
Fe-doping
Ultralow OER overpotential

ABSTRACT

Electrochemical water splitting remains a long way from large-scale practical application due to the fact that the catalytic efficiency cannot satisfy the requirement, and thus reasonable design catalyst is particularly essential. Herein, a heteroatom-doped heterogeneous interfacial catalyst (Fe-CoN/CoS₂) has been successfully synthesized by nitridation and sulfidation process for water electrolysis. Strikingly, an ultralow OER overpotential (154 mV) at 10 mA·cm⁻² for OER is achieved. Meanwhile, Fe-CoN/CoS₂ is of low HER overpotentials of 72 and 39 mV to drive current density of 10 mA·cm⁻² in alkaline and acid condition, respectively. Furthermore, the electrolytic cell assembled with Fe-CoN/CoS₂ drives a voltage of 1.48 V at 10 mA·cm⁻². The doping of Fe can further reinforce the interaction of heterointerface between CoN and CoS₂, resulting in the interfacial coupling enhancement. Density functional theory (DFT) calculations verify the Fe-doping can alter the electronic structure around the heterointerface and boosts the intrinsic catalytic activity, thus reduces the adsorption energy barriers about H* and oxygen-containing intermediates. This work provides a significant insight into the understanding of transition metal ion-doping heterointerface for facilitating the catalytic activity.

1. Introduction

The global world has seen a stunning rise in the rate of energy demand over the past few decades [1,2]. The depletion of fossil fuel is tipping our world towards severe energy crunch [3,4]. Therefore, searching for new energy sources is crucial to the sustainable development of mankind [5–7]. Across all the renewable energy sources, the most desirable one is hydrogen by virtue of its zero-pollution and high energy density [8,9]. Of all the approaches of producing hydrogen, electrolysis of water catches the researchers' attention for the reason that it is high utilization and no by-products [10]. Electrochemical water splitting encompasses two half-reactions: hydrogen evolution reaction (HER) in cathode and oxygen evolution reaction (OER) in anode [11–14]. Noble metal catalysts (Pt, Pd, Ru, Ir) hold the good activity to HER and OER, but their current enormous cost makes them hard for application in industry [15,16]. Thus, it matters that researchers develop high-efficient and inexpensive electrocatalysts for electrochemical water splitting [17–19].

OER has a vital role to play in overall water splitting since most of energy consumption comes from it, so reducing OER overpotential has become a hot topic [20–23]. Today numerous available catalyst preparation strategies for OER have been summarized by researchers and applied in the experimental design [24–27]. The first is doping engineering [28]. For example, Zhang et al. synthesized a Fe and Mo-doping Ni₃S₂ on NF (FeMo-Ni₃S₂/NF) via one-pot hydrothermal method, which exhibited overpotential of 180 mV at 10 mA·cm⁻² for OER [29]. Zhu et al. manufactured Er-doping NiFe-LDH (Er-NiFe-LDH/NF) and it needed only 191 mV to reach current density of 10 mA·cm⁻² [30]. The second is interfacial engineering [31,32]. One noticeable example is by Chen et al., who fabricated a MoS₂/CoS/NF catalyst and it showed a small overpotential of 207 mV and 67 mV at 10 mA·cm⁻² for OER and HER [33]. In short, researchers have made some big progress based on these strategies [34].

As is widely known, there are many merits about heterostructure [35,36]. Heterostructure can endow catalysts with superior active sites due to the lattice strain [35]. The charge transfer and synergistic effect

* Corresponding authors.

E-mail addresses: herx@swu.edu.cn (R. He), suwm@163.com (W. Su), liming@swu.edu.cn (M. Li).

<https://doi.org/10.1016/j.apcatb.2023.122928>

Received 9 March 2023; Received in revised form 3 May 2023; Accepted 28 May 2023

Available online 29 May 2023

0926-3373/© 2023 Elsevier B.V. All rights reserved.

between different sections can boost the efficiency of chemical reaction [37]. The component design of heterostructure is flexible [38]. Based on these properties of heterogeneous interfaces, great strides in heterostructure catalysts without precious metals are acquired [39]. Zeng et al. fabricated a $\text{Ni}_2\text{P}/\text{Ni}_3\text{S}_2$ heterogeneous structure with strong coupling effects, which displayed a better electrolytic water performance than pure Ni_3S_2 [40]. Yet on the basis of heterogeneous structure, it is very crucial to regulate the heterogeneous structure in a reasonable and effective way to further improve the electrocatalytic activity. On that note, only a small number of efforts has been devoted to this [41–43]. Particularly, doping strategy is an effective method to regulate the heterogeneous interface. A study from Cao et al. demonstrated a doped heterostructure ($\text{Co-NiS}_2/\text{MoS}_2$) can decrease the energy barrier about water splitting, displaying superior electrocatalytic activity ($\eta_{20} = 283$ mV for OER; $\eta_{10} = 89$ mV for HER) compared to pure $\text{NiS}_2/\text{MoS}_2$ ($\eta_{20} = 344$ mV for OER; $\eta_{10} = 106$ mV for HER) [42]. Tang et al. exhibited a Fe-doped heterostructure ($\text{Fe-NiTe-Ni}_{12}\text{P}_5$) can modulate the binding strength about OER intermediates to enhance the OER performance ($\eta_{50} = 303$ mV), and this value is much lower than pure $\text{NiTe-Ni}_{12}\text{P}_5$ ($\eta_{50} = 385$ mV) [44]. These works have given a valid proof that the heterostructure via foreign atoms-doping can further promote electrocatalytic performance compared to pure heterostructure. However, the impact of the introduction of foreign atoms on heterostructures has not been known until now, and this is of great significance for us to understand how doping affects the catalytic mechanism of heterogeneous interfaces and the rational and controllable design of such materials. Meanwhile, the electrocatalytic performance, especially OER performance, should be further upgraded to meet the actual application requirement.

Herein, a novel Fe doped cobalt nitride/cobalt sulfide catalyst ($\text{Fe-CoN}/\text{CoS}_2$) was fabricated successfully via first hydrothermal process, then nitridation and finally partial sulfidation. X-ray photoelectron spectroscopy (XPS) verified the Fe-doping can enhance the interaction between the two components of the heterogeneous interface, optimize the electron distribution near the interface and significantly improves the inherent catalytic activity of the catalyst, resulting in interfacial coupling enhancement. This interfacial coupling enhancement can directly entitle $\text{Fe-CoN}/\text{CoS}_2$ to excellent electrocatalytic performance, especially for OER. As expected, $\text{Fe-CoN}/\text{CoS}_2$ displays an ultralow OER overpotential ($\eta = 154$ mV) at $10 \text{ mA}\cdot\text{cm}^{-2}$ in alkaline condition. On the other hand, the $\text{Fe-CoN}/\text{CoS}_2$ shows 72 mV and 39 mV of overpotentials at $10 \text{ mA}\cdot\text{cm}^{-2}$ for HER in alkaline and acid condition, respectively. DFT calculations demonstrate that the introduction of Fe can change the charge distribution on the heterointerface and enhance the conductivity, resulting in the optimal adsorption of oxygen-containing intermediates ($^*\text{OH}$, $^*\text{O}$ and $^*\text{OOH}$) for OER and H^* for HER. This work lays a foundation for the modification of heterogeneous interfacial catalysts and paves the way for studying the mechanism of doping on heterointerface.

2. Experimental section

2.1. Materials

KOH, ethanol ($\text{C}_2\text{H}_5\text{OH}$), sublimed sulfur, perchloric acid (HClO_4) and HNO_3 were ordered from Chongqing Chuandong Chemical (Group) Co., Ltd. $\text{Co}(\text{NO}_3)_2\cdot 6\text{H}_2\text{O}$, $\text{Fe}(\text{NO}_3)_3\cdot 9\text{H}_2\text{O}$, Nafion and urea ($\text{CH}_4\text{N}_2\text{O}$) were supplied by Aladdin. RuO_2 , Pt/C, nickel foam (NF) and carbon paper (CP) were obtained from Hesenbio Ltd. (China). NH_4F was purchased from Shanghai Titanchem Co., Ltd.

2.2. Synthesis of Fe doped Co precursor (Fe-Co precursor)

The hydrophilic properties of carbon paper were obtained by pre-treating it with concentrated HNO_3 . A hydrothermal method was used to synthesize the Fe-Co precursor. 1 mmol $\text{Co}(\text{NO}_3)_2\cdot 6\text{H}_2\text{O}$, 0.15 mmol $\text{Fe}(\text{NO}_3)_3\cdot 9\text{H}_2\text{O}$, 300 mg urea and 300 mg NH_4F were dissolved in 15 mL deionized water and it was transferred into a 30 mL Teflon-lined

autoclave. Then a piece of hydrophilic CP ($2 \times 3 \text{ cm}^2$) was immersed in this solution. During the hydrothermal process, the temperature was 120°C , and the duration was 6 h. Following the reaction, the CP was cleaned with abundant deionized water to obtain Fe-Co precursor.

2.3. Synthesis of Fe doped CoN (Fe-CoN)

In order to produce Fe-CoN, a nitridation process was used. A porcelain boat containing 1.0 g urea was placed in the upstream of a tube furnace while a boat containing Fe-Co precursor was placed in the downstream. The furnace was heated to 400°C ($5^\circ\text{C}/\text{min}$) for 3 h under Ar atmosphere. Once cooled to room temperature, Fe-CoN was collected.

2.4. Synthesis of Fe-CoN/ CoS_2

$\text{Fe-CoN}/\text{CoS}_2$ was synthesized by partial sulfuration. 0.5 g sublimed sulfur was put into a porcelain boat and it was placed in the upstream of the tube furnace. The Fe-CoN was placed in the downstream. The furnace was heated to 300°C ($5^\circ\text{C}/\text{min}$) for 2 h under Ar atmosphere. As soon as it reached room temperature, Fe-CoN/ CoS_2 was collected. The synthesis of 20%Fe-CoN/ CoS_2 (Fe:Co = 0.2: 1) or 10%Fe-CoN/ CoS_2 (Fe:Co = 0.1: 1) was the same as Fe-CoN/ CoS_2 except that the amount of $\text{Fe}(\text{NO}_3)_3\cdot 9\text{H}_2\text{O}$ was 0.2 or 0.1 mmol. The mass loading was $1.7 \text{ mg}\cdot\text{cm}^{-2}$ on the CP.

2.5. Synthesis of the control samples

The synthesis of CoN/ CoS_2 was the same as Fe-CoN/ CoS_2 except that $\text{Fe}(\text{NO}_3)_3\cdot 9\text{H}_2\text{O}$ was not added. The Fe- CoS_2 was synthesized via a sulfuration process: 0.5 g sublimed sulfur was put into a porcelain boat and it was placed in the upstream of the tube furnace and the Fe-Co precursor was placed in the downstream, then the furnace was heated to 300°C ($5^\circ\text{C}/\text{min}$) for 2 h under Ar atmosphere, finally after cooled to the room temperature, the Fe- CoS_2 was obtained. The synthesis of CoN and CoS_2 were the same as Fe-CoN and Fe- CoS_2 , respectively, except that $\text{Fe}(\text{NO}_3)_3\cdot 9\text{H}_2\text{O}$ was not added.

2.6. Preparation of Fe-CoN/ CoS_2 on NF

We scraped Fe-CoN/ CoS_2 powder off the CP loaded by Fe-CoN/ CoS_2 . Then, 5 mg Fe-CoN/ CoS_2 powder was dispersed into a mixture contained 400 μL ethanol, 100 μL deionized water and 10 μL Nafion to form an ink via ultrasonication for 0.5 h. The NF was washed by ethanol, 3 M HCl and deionized water via sonication for 30 min to remove the impurities on the surface. At last, 170 μL of this ink was dropped onto NF ($1 \times 1 \text{ cm}^2$). The mass loading was $1.7 \text{ mg}\cdot\text{cm}^{-2}$.

2.7. Preparation of Pt/C and RuO_2 electrodes

5 mg Pt/C or RuO_2 was dispersed into a mixture contained 400 μL ethanol, 100 μL deionized water and 10 μL Nafion to form an ink via ultrasonication for 0.5 h. Then, 170 μL of this ink was dropped onto CP ($1 \times 1 \text{ cm}^2$). The mass loading was the same as Fe-CoN/ CoS_2 .

2.8. Characterization

The XRD data was tested via Bruker D2 PHASER (Germany) with $\text{Cu K}\alpha$ radiation ($\lambda \approx 0.1542 \text{ nm}$). The XPS data of all samples were obtained by the Thermo Scientific K-Alpha (Al $\text{K}\alpha$ radiation, USA). The scanning electron microscope (SEM) data was tested by FlexSEM 1000II, (Japan). Transmission electron microscope (TEM) data was measured by ZEISS GeminiSEM 300 (Germany). Raman tests were carried out using the Thermo Fischer DXR Raman spectrometer.

2.9. Electrochemical tests

We tested the electrochemical performances of all samples using CHI 760 (CH Instrument, China). The OER test was only studied in alkaline condition (1.0 M KOH). And the HER test was studied in acidic (1.0 M HClO₄) and alkaline condition (1.0 M KOH), respectively. A three-electrode setup was used: a graphite rod (counter electrode), the as-prepared catalysts (working electrode) and a Hg/HgO electrode or an Ag/AgCl electrode (reference electrodes). The scan rate of all the LSV tests was 2 mV·s⁻¹. The electrochemical double-layer capacitances (*C_{dl}*) was assessed via CV method. Chronoamperometry (CA) method was employed to evaluate the durability of our catalysts. Electrochemical impedance spectroscopy (EIS) data was collected on Autolab (PGSTAT302N, Switzerland) and the frequency was from 10⁵ to 0.1 Hz. All potentials in this work were converted to RHE as follow:

$$E(\text{RHE}) = E(\text{Hg/HgO}) + 0.908 \text{ V (In alkaline condition)}$$

$$E(\text{RHE}) = E(\text{Ag/AgCl}) + 0.215 \text{ V (In acidic condition)}$$

2.10. Computation methods

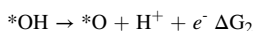
All density functional theory (DFT) calculations were performed on the Vienna Ab-initio Simulation Package (VASP) software. The electron-ion interactions were described via the projected augmented wave (PAW) [45–48]. The exchange and correlation of electron were represented by the generalized gradient approximation (GGA) combined with Perdew–Burke–Ernzerhof (PBE) functional [49,50]. A cut-off energy of 400 eV was used for optimization. The Monkhorst-Pack K point mesh was $1 \times 2 \times 1$ [51]. All structures were optimized until the energy converged to 10⁻⁵ eV and force converged to 0.02 eV/Å [52]. Periodic interactions were eliminated by adding a vacuum layer of 15 in the c direction.

For HER process, the Gibbs free energy change (ΔG_{H^*}) was computed as follow:

$$\Delta G_{\text{H}^*} = \Delta E(\text{H}^*) + \Delta E(\text{zpe}) - T\Delta S$$

where $\Delta E(\text{H}^*) = E(\text{slab}+\text{H}^*) - E(\text{slab}) - 1/2E(\text{H}_2)$, $\Delta E(\text{zpe})$ is the change of zero-point energy and ΔS is the change of entropy. In this work, a value of 0.24 eV was used to approximate $\Delta E(\text{zpe}) - T\Delta S$ based on the previous work [53].

The OER process can be displayed as follow: [54,55].



where, * represents active site, and OH*, O*, OOH* are three intermediates of OER. The ΔG_i of OER can be calculated by the following equation:

$$\Delta G_i = \Delta E + \Delta E(\text{zpe}) - T\Delta S \quad (i = 1, 2, 3, 4)$$

where ΔE is the adsorption energy of intermediate and $\Delta E(\text{zpe})$, ΔS are calculated based on vibrational frequencies via VASPKIT [56]. The theoretical overpotential can be expressed as follow:

$$\eta = \text{Max} [\Delta G_1, \Delta G_2, \Delta G_3, \Delta G_4]/e - 1.23 \text{ V}$$

3. Results and discussion

3.1. Catalysts synthesis and physical characterizations

The general synthesis scheme of Fe-CoN/CoS₂ is exhibited in Scheme. 1. First, a Fe-Co precursor was obtained by a simple hydro-thermal process. The subsequent nitridation using with urea was carried out to form Fe-CoN. At last, Fe-CoN/CoS₂ was synthesized successfully via partial sulfidation of Fe-CoN.

The composition of all catalysts was evaluated by XRD. As shown in Fig. S1, the XRD pattern of Fe-Co precursor matches well with Co(OH)F (PDF#41–1487). In Fig. 1a, the peaks at 36.3°, 42.2° and 61.4° can be indexed to the (111), (200) and (220) planes of CoN (PDF#16–0116) [57], respectively. Meanwhile, the peaks at 32.3°, 36.3°, 46.5° and 54.7° are in good agreement with (200), (210), (220) and (311) planes of CoS₂ (PDF#41–1471) [58], respectively. There is a sharp peak at 26.6°, resulting from the CP. Hence, the XRD pattern of Fe-CoN/CoS₂ without any miscellaneous peaks proves that it consists only of CoN and CoS₂. It is worth noting that no peak position shift exists in XRD patterns before (CoN/CoS₂) and after Fe doping (Fe-CoN/CoS₂), which is attributed to the fact that the atomic radius of Co and Fe are almost the same. Similarly, the XRD patterns of the different Fe-doping (20%Fe-CoN/CoS₂ and 10%Fe-CoN/CoS₂) are in line with Fe-CoN/CoS₂, indicating the different doping amounts of Fe cannot change the phase composition (Fig. S2). For the contrast, The XRD patterns of Fe-CoN, CoN, Fe-CoS₂ and CoS₂ were also studied (Fig. S3). The peaks of Fe-CoN and CoN correspond to CoN (PDF#16–0116), while the peaks of Fe-CoS₂ and CoS₂ are in accordance with CoS₂ (PDF#41–1471). Likewise, Fe doping does not generate peak shift. All of the XRD results confirm that Fe doping has no effect on the phase composition of the heterogeneous interface.

Fig. 1b–c and Fig. S4–8 display the SEM images of Fe-CoN/CoS₂, CoN/CoS₂, Fe-CoN, CoN, Fe-CoS₂ and CoS₂, respectively. In Fig. S4, S6 and S8, the CoN/CoS₂, CoN and CoS₂ exhibit a nanorod structure and these nanorod clump together to form a shape similar to a pinecone. After the addition of Fe element, the morphology is transformed into nanosheet (Fig. 1b–c, S5 and S7), implying the doping of Fe has great influence on the microstructure of catalysts, which is similar to the previous work [59]. It should be stressed that the nitridation and vulcanization make no effect on the morphology.

The microstructure of Fe-CoN/CoS₂ was further explored via TEM. The TEM images of Fe-CoN/CoS₂ at low resolution (Fig. 1d–e) exhibit it is nanosheet morphology, which fit in with the SEM results. HRTEM image (Fig. 1f) reveals the inter-planar spacing of 0.25 nm and 0.21 nm can be ascribed to the (111) and (200) planes of CoN, while the inter-planar spacing of 0.27 nm can be indexed to the (200) plane of CoS₂. There is a distinct grain boundary (Blue dotted line) between CoN and CoS₂, successfully suggesting the existence of heterogeneous interface in Fe-CoN/CoS₂. Similarly, the SAED pattern (Fig. 1g) exhibits some clear diffraction rings, which is in conformity with the (111) plane of CoN and the (200), (211) and (220) planes of CoS₂. Furthermore, the distribution of elements is determined by HAADF-STEM and EDS-mapping measurements (Fig. 1h). The elements of Fe, Co, N and S are distributed homogeneously in the entire Fe-CoN/CoS₂ nanosheet.

To further investigate how Fe doping affects heterogeneous interface, the XPS analysis was used. Fig. 2a shows the XPS survey spectrum of Fe-CoN/CoS₂, and the elements of Co, Fe, N and S exist in it. The emergence of Fe 2p peak confirms the Fe element is successfully doped into the catalyst. It is noted that the element of O is derived from the oxidation of the sample by air, while the element of C belongs to CP. In the Co 2p spectrum (Fig. 2b) of pristine CoN, the peaks of 795.80 and 779.80 eV can assign to Co 2p_{1/2} and Co 2p_{3/2}, respectively, and the N 1s peak of pristine CoN (Fig. 2c) is at 398.65 eV, which can assign to Co–N bond. Fig. 2d exhibits the peaks of 795.52 and 779.65 eV correspond to Co 2p_{1/2} and Co 2p_{3/2} of pristine CoS₂, respectively. Fig. 2e presents the peaks of S 2p_{1/2} and S 2p_{3/2} are 164.01 and 162.81 eV, respectively,

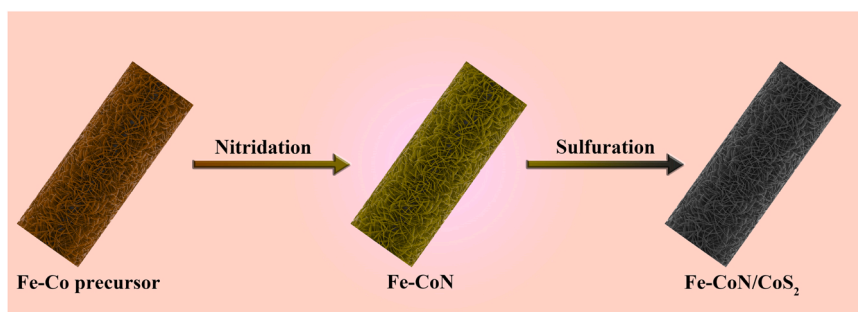
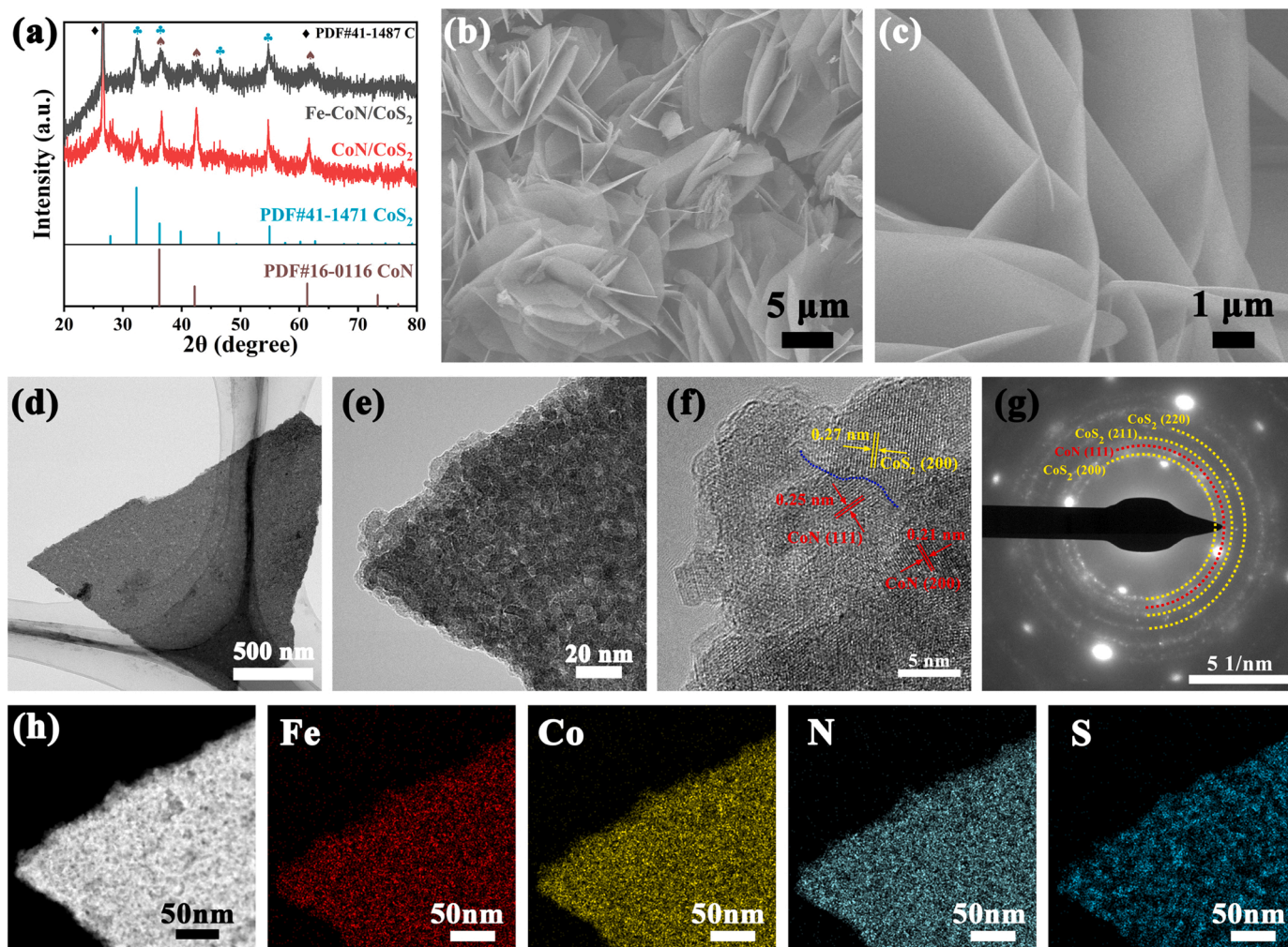
Scheme 1. synthesis scheme of Fe-CoN/CoS₂.

Fig. 1. (a) The XRD patterns of Fe-CoN/CoS₂ and CoN/CoS₂. (b-c) SEM images of Fe-CoN/CoS₂. (d-f) TEM and HRTEM images of Fe-CoN/CoS₂. (g) Selected area electron diffraction (SAED) pattern of Fe-CoN/CoS₂. (h) HAADF-STEM image and corresponding EDS-mapping images of Fe-CoN/CoS₂.

while the signal at 168.58 eV is coming from the SO_x²⁻ because of the oxidation by air.

After the formation of heterogeneous interface between CoN and CoS₂, the peaks of Co 2p_{1/2} and Co 2p_{3/2} about CoN/CoS₂ are 796.30 and 780.29 eV, respectively, which are positively shifted by 0.50 and 0.49 eV, respectively, compared to pristine CoN (Fig. 2b), and those of CoN/CoS₂ are positively shifted by 0.78 and 0.64 eV, respectively, compared to pristine CoS₂ (Fig. 2d). Meanwhile, the N 1 s peak of CoN/CoS₂ is located at 398.03 eV, which is negatively shifted by 0.62 eV compared with pristine CoN (Fig. 2c). The peaks of S 2p_{1/2} and S 2p_{3/2} about CoN/CoS₂ are at 163.64 and 162.44 eV, and both are negatively

shifted by 0.37 eV compared to pristine CoS₂ (Fig. 2e). These results prove a phenomenon that the formation of heterogeneous interfaces can lead to interface polarization.

When Fe was doped into the pristine CoN, the Co 2p_{1/2} and Co 2p_{3/2} peaks of Fe-CoN are separately shifted by 0.39 and 0.38 eV positively and the N 1 s peak are negatively shifted by 0.31 eV relative to pristine CoN. At the same time, when Fe was doped into the pristine CoS₂, the corresponding peaks of Co 2p_{1/2} and Co 2p_{3/2} about Fe-CoS₂ are separately shifted by 0.32 and 0.46 eV positively and the peaks of S 2p_{1/2} and S 2p_{3/2} of Fe-CoS₂ both are shifted by 0.15 eV negatively relative to pristine CoS₂. This result suggests a part of Fe electron is transferred to

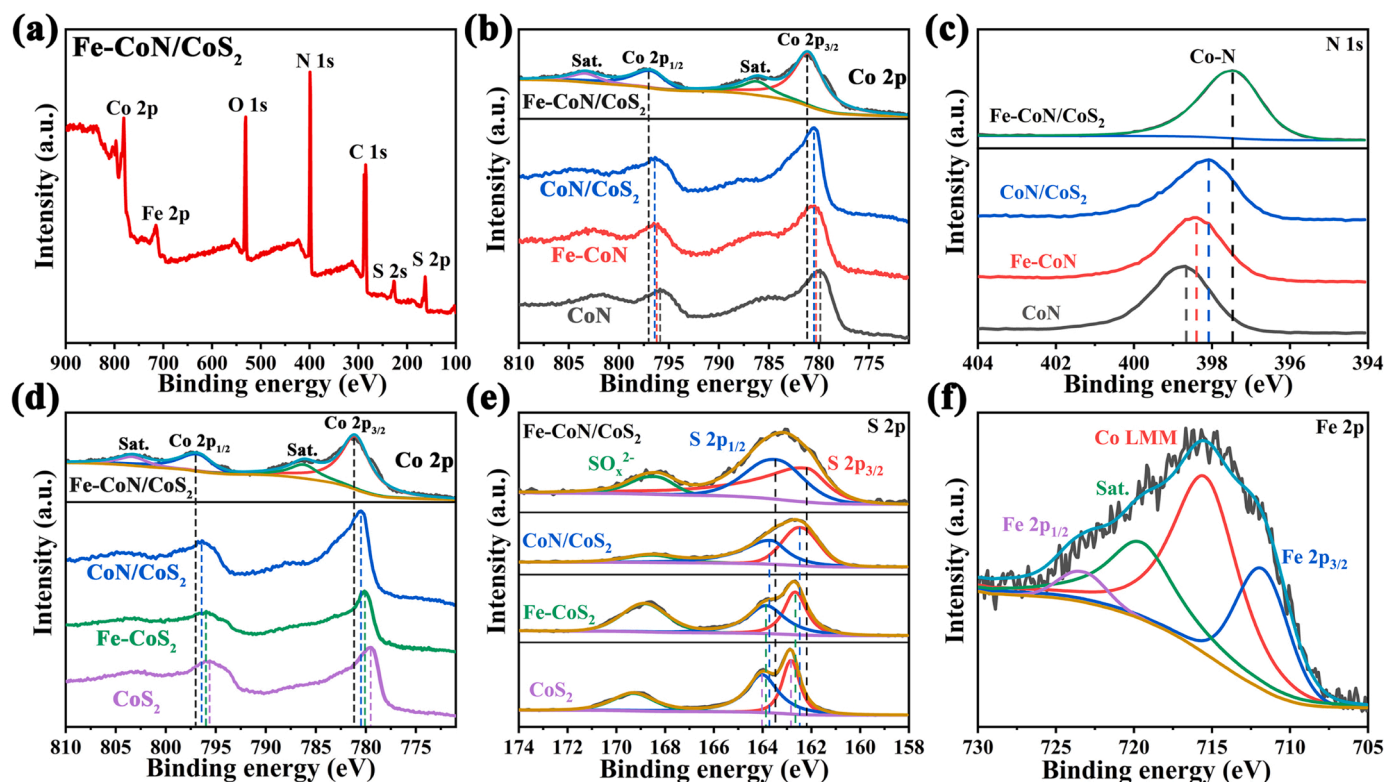


Fig. 2. XPS survey spectrum and the high-resolution XPS spectra of Fe-CoN/CoS₂: Co 2p, N 1s, S 2p and Fe 2p.

Co as a result of the difference of electronegativity between the two atoms, which makes left shift of Co peaks and right shift of N and S peaks.

Yet take a moment to look beyond this, there is a weird phenomenon from the XPS analysis of Fe-CoN/CoS₂. The Co 2p spectrum of Fe-CoN/CoS₂ displays two main peaks at 796.84 and 781.03 eV, which corresponds to Co 2p_{1/2} and Co 2p_{3/2}. Compared with pure heterostructure (CoN/CoS₂), the Co 2p_{1/2} and Co 2p_{3/2} peaks of Fe-CoN/CoS₂ further move by 0.54 and 0.74 eV positively. In Fig. 2c, the peak of Fe-CoN/CoS₂ located at 397.41 eV can be assigned to N 1s, which is further shifted by 0.62 eV negatively compared to the CoN/CoS₂. Meanwhile, the peaks of S 2p_{1/2} and S 2p_{3/2} are 163.40 and 162.20 eV, respectively, and both are negatively shifted by 0.24 eV compared to the CoN/CoS₂ (Fig. 2e). These results mean that the doping of Fe can further intensify the interaction of heterointerface between CoN and CoS₂ and further polarize the electron vigorously, resulting in more charge shift. Meanwhile, it optimizes the electron distribution near the interface and significantly improves the inherent catalytic activity of the catalyst. We believe that this strong interfacial polarization is attributed to a dopant-induced interfacial coupling enhancement effect. Obviously, this dopant-induced interfacial coupling enhancement effect can bring better catalytic activity and conductivity to the catalyst, which will be fully proved in the following electrochemical tests. The Fe 2p spectrum is shown in Fig. 2f. Noticeably, there is a peak of 715.43 eV, which attributes to Co LMM Auger peak [60,61]. The peaks at 723.20 and 711.77 eV can separately ascribe to the Fe 2p_{1/2} and Fe 2p_{3/2}, suggesting the existence form of Fe in the catalyst is Fe³⁺ [61].

3.2. OER performance

We first tested the OER properties of all catalysts. Fig. 3a exhibits the LSV curves of our samples and Fig. 3b displays the corresponding overpotentials at 10 and 100 mA·cm⁻². Pristine CoS₂ and CoN present high overpotentials of 273 and 286 mV at 10 mA·cm⁻², respectively, indicating their poor OER activity. After Fe doping, the overpotentials of

Fe-CoS₂ and Fe-CoN reduce to 252 and 280 mV, suggesting the electron transfer caused by Fe doping can entitle the material to a better OER activity but not obvious. When the formation of heterointerface (CoN/CoS₂) between CoS₂ and CoN, the overpotential was improved to 237 mV, indicating there is synergistic effect between CoS₂ and CoN and this synergistic effect can significantly enhance the performance of OER. These results demonstrate the heteroatom doping or the formation of heterointerface can result in superior OER activity. However, after Fe doping into the heterointerface, the formed catalyst (Fe-CoN/CoS₂) shows an ultra-low overpotential of 154 mV at 10 mA·cm⁻² and a similar trend is shown at high current densities. This value is much smaller than most recently reported OER catalysts without precious metals (Table S1). This result confirms the dopant-induced interfacial coupling enhancement can further boost the intrinsic catalytic activity of the heterointerface and improve the electronic conductivity, thus extremely upgrading the OER performance of the catalyst. Furthermore, Fe-CoN/CoS₂ with different Fe ratios for OER performance were also measured (Fig. S9). Similarly, Fe-CoN/CoS₂ presents the optimal OER performance among them (20%Fe-CoN/CoS₂, Fe-CoN/CoS₂ and 10%Fe-CoN/CoS₂).

Fig. 3c shows the Tafel slope of Fe-CoN/CoS₂ is only 71 mV·dec⁻¹, and this value is less than CoN/CoS₂ (87 mV·dec⁻¹), Fe-CoS₂ (124 mV·dec⁻¹), CoS₂ (125 mV·dec⁻¹), Fe-CoN (170 mV·dec⁻¹) and CoN (182 mV·dec⁻¹). This represents the dopant-induced interfacial coupling enhancement can not only lead to outstanding catalytic activity to the catalyst, but also significantly promote the catalytic kinetics. Furthermore, for all samples, the active sites can be studied by C_{dl} measured from CV at different scan rates. Fig. 3d exhibits the maximum C_{dl} value is 321 mF·cm⁻² for the Fe-CoN/CoS₂ (Fig. S10), demonstrating the dopant-induced interfacial coupling enhancement can trigger high ECSA than other catalysts, which undoubtedly causes the optimal electrocatalytic activity. EIS test (Fig. 3e) displays the smallest semicircular region for the Fe-CoN/CoS₂, i.e. 1.97 Ω, and this value is the smallest among all samples (Table S2), representing this interfacial coupling enhancement can result in a faster charge transfer during the OER process, thus improving the electron conductivity. Chronoamperometry test (Fig. 3f)

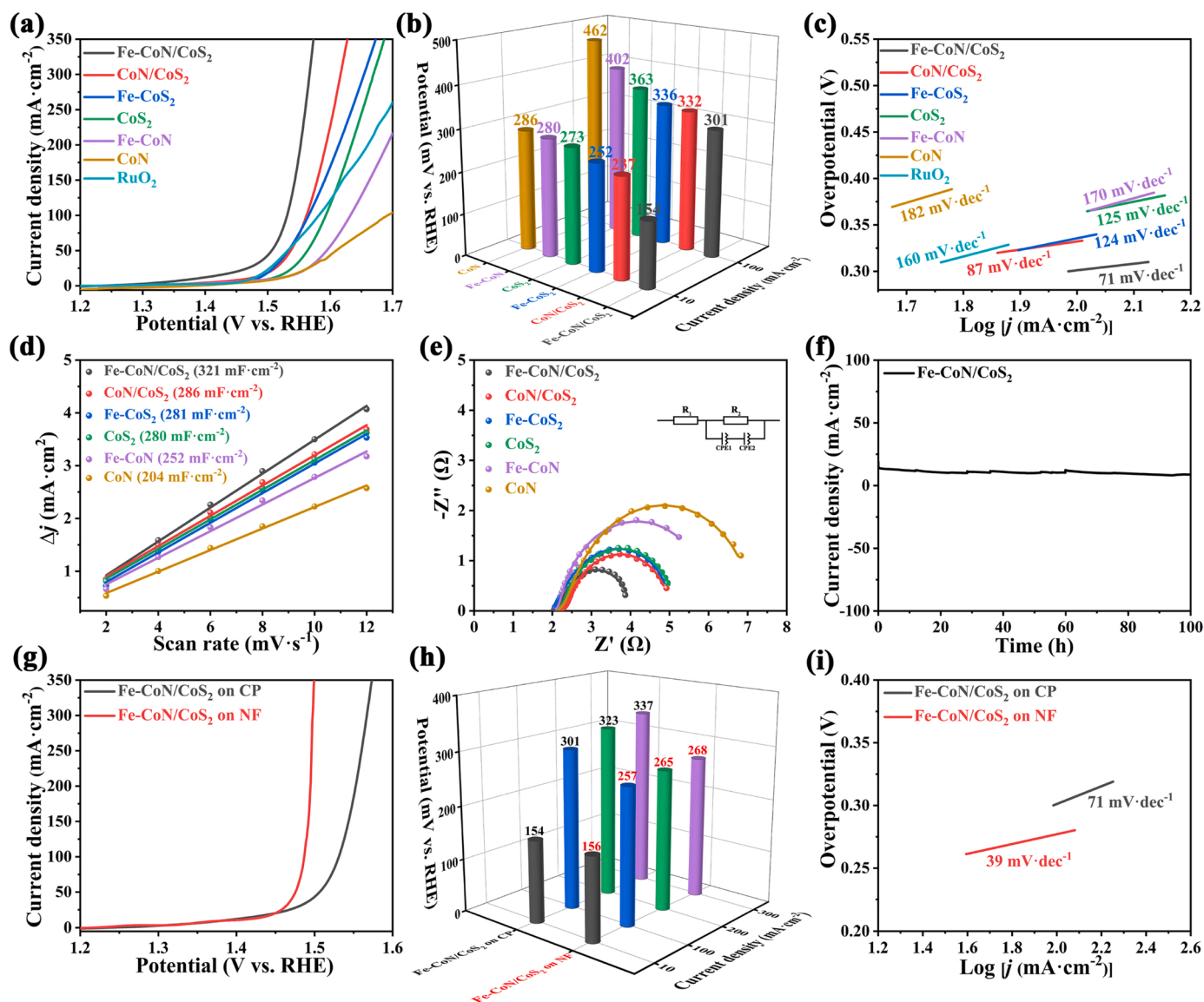


Fig. 3. In 1 M KOH, (a) LSV curves of OER. (b) Corresponding overpotentials at 10 and 100 $\text{mA}\cdot\text{cm}^{-2}$. (c) Tafel plots. (d) C_{dl} of the as-prepared catalysts. (e) Nyquist plots. (f) i-t curve of Fe-CoN/CoS₂ at constant potential. (g) The LSV curve comparisons of Fe-CoN/CoS₂ on CP and Fe-CoN/CoS₂ on NF for OER in 1 M KOH. (h) The overpotential comparisons at 10, 100, 200 and 300 $\text{mA}\cdot\text{cm}^{-2}$. (i) Corresponding Tafel plots.

shows the fluctuation in current density is almost negligible for 100 h, confirming the Fe-CoN/CoS₂ has outstanding durability for OER. To elucidate the influence of content of Fe in the catalyst on stability, the LSV curves were compared between pre and post the stability test. As displayed in Fig. S11, the overpotentials of 10%Fe-CoN/CoS₂, Fe-CoN/CoS₂, 20%Fe-CoN/CoS₂ at 10 $\text{mA}\cdot\text{cm}^{-2}$ only present small increases of 7, 6 and 8 mV, respectively, while the CoN/CoS₂ shows an increase of 12 mV, indicating the Fe has an essential role to play in the stability of the heterointerface.

From the above analysis, we can conclude that the Fe-CoN/CoS₂ possesses excellent OER intrinsic activity, but the performance of Fe-CoN/CoS₂ is not very satisfactory at high current density, such as $\eta_{100} = 301$ mV. About this, an explanation may be found on a more suitable substrate. Thus, the Fe-CoN/CoS₂ powder is scraped off the CP loaded by catalyst carefully, then it is made into ink to drop onto the pre-treated NF. Fig. 3g presents the LSV comparisons between Fe-CoN/CoS₂ on CP and Fe-CoN/CoS₂ on NF. At low current density, the OER performance of Fe-CoN/CoS₂ on NF ($\eta_{10} = 156$ mV) is the same as Fe-CoN/CoS₂ on CP ($\eta_{10} = 154$ mV), which proves that the inherent intrinsic activity of the Fe-CoN/CoS₂ is not changed. However, as the current density reaches

100, 200 and 300 $\text{mA}\cdot\text{cm}^{-2}$, the corresponding overpotentials of Fe-CoN/CoS₂ on NF are only 257, 265 and 268 mV, which greatly exceeds the OER performance of Fe-CoN/CoS₂ on CP at the same current density (Fig. 3h), confirming the Fe-CoN/CoS₂ has better OER activity on a more suitable substrate (NF). In addition, the Tafel slope (Fig. 3i) of Fe-CoN/CoS₂ on NF (39 $\text{mV}\cdot\text{dec}^{-1}$) is also lower than Fe-CoN/CoS₂ on CP (71 $\text{mV}\cdot\text{dec}^{-1}$), suggesting the Fe-CoN/CoS₂ can accelerate the reaction on a more suitable substrate, showing a faster catalytic reaction kinetics.

After the OER stability test, the change of surface morphology and structure of Fe-CoN/CoS₂ were also investigated. As displayed in Fig. S12, the nanosheet structure is roughly maintained. A little bit different is that the nanosheets after stability test are more fragmented due to the constant impact of O₂ bubbles on the catalyst surface. The composition of the Fe-CoN/CoS₂ after OER test was characterized by Raman spectrum and XPS. Many previous works have reported that cobalt-based electrocatalysts undergo partial oxidation and reconstruction to generate corresponding oxyhydroxide (CoOOH) during the OER process [62,63]. As shown in Fig. S13, the peak at 524 cm^{-1} can be assigned to the Co-O symmetric stretching, while the peak at 578 cm^{-1} can ascribe to the tensile vibration of Co-OH, which is consistent with

previous report [64]. The peak at 605 cm^{-1} is the characteristic peak of CoOOH [65]. Meanwhile, there is a sharp peak located at 644 cm^{-1} , which is related to the Co-OOH [66]. These results demonstrate the Fe-CoN/CoS₂ during the OER process is transformed into the CoOOH partially.

To further certify the existence of CoOOH after OER test, XPS spectrum was employed. In Fig. S14a, the survey spectrum proves the existence of Co, Fe, O, N, C and S. In Fig. S14b, the peaks at 780.5 and 795.68 eV can be ascribed to the Co³⁺, while the peaks at 782.00 and 797.18 can be assigned to the Co²⁺. The peaks at 533.61, 531.61 and 529.97 eV in Fig. S14c are belonging to the absorbed H₂O, O-H and Co-O bond, respectively [67]. There is a large amount of Co-O and O-H bonds in O 1 s spectrum, further confirming the formation of CoOOH. In the S 2p spectrum (Fig. S14d), the peaks of S 2p_{1/2} and S 2p_{3/2} are 163.40 and 162.20 eV, respectively, which are the same as the initial Fe-CoN/CoS₂, while the peaks of 166.42 and 167.69 eV can be assigned to SO_x²⁻ [58]. In the original Fe-CoN/CoS₂, the intensity of S 2p_{1/2} and S 2p_{3/2} is much bigger than SO_x²⁻, but after the OER test, the intensity of S 2p_{1/2} and S 2p_{3/2} is much smaller than SO_x²⁻, indicating the element of S is partially oxidized to the SO_x²⁻. Similarly, the N 1 s peak (Fig. S14e) becomes weak compared to the initial Fe-CoN/CoS₂ [62]. However, the all peak positions (715.43 eV for Co LMM, 723.20 and 711.77 eV for Fe 2p_{1/2} and Fe 2p_{3/2}) of Fe (Fig. S14f) are the same as the initial Fe-CoN/CoS₂, indicating the Fe element still exists as Fe³⁺. All the XPS and Raman results demonstrate the Fe-CoN/CoS₂ was partially oxidized to CoOOH during OER.

3.3. HER performance

The electrocatalytic HER performances of all samples were first assessed in acidic condition. In Fig. 4a-b, Fe-CoN/CoS₂ exhibits a small overpotential of 39 mV at $10\text{ mA}\cdot\text{cm}^{-2}$, which is very close to Pt/C (24 mV) and exceeds most recently reported catalysts (Table S3). By contrast, the overpotentials of CoN/CoS₂ (52 mV), Fe-CoS₂ (82 mV) and CoS₂ (110 mV) are much higher than Fe-CoN/CoS₂ at the same current

density, and it is the same trend at higher current density. These HER performances indicate that the dopant-induced interfacial coupling enhancement is beneficial to enhance the intrinsic HER activity, thus boosting the HER performance. It should be noted that Fe-CoN and CoN have no HER performances because they are unstable under acidic condition. Moreover, the HER performances in 1 M HClO₄ of Fe-CoN/CoS₂ with different Fe ratios are exhibited in Fig. S15, and the Fe-CoN/CoS₂ also shows the lowest overpotential and Tafel slope.

In Fig. 4c, the Fe-CoN/CoS₂ presents a low Tafel slope ($42\text{ mV}\cdot\text{dec}^{-1}$), and it is lower than CoN/CoS₂ ($49\text{ mV}\cdot\text{dec}^{-1}$), Fe-CoS₂ ($53\text{ mV}\cdot\text{dec}^{-1}$), CoS₂ ($56\text{ mV}\cdot\text{dec}^{-1}$), Fe-CoN ($226\text{ mV}\cdot\text{dec}^{-1}$) and CoN ($259\text{ mV}\cdot\text{dec}^{-1}$), indicating Fe-CoN/CoS₂ is of faster kinetics for HER due to the interfacial coupling enhancement. In Fig. 4d, Fe-CoN/CoS₂ shows the largest C_{dl} value of $202\text{ mF}\cdot\text{cm}^{-2}$ in comparison of CoN/CoS₂ ($194\text{ mF}\cdot\text{cm}^{-2}$), Fe-CoS₂ ($175\text{ mF}\cdot\text{cm}^{-2}$), CoS₂ ($164\text{ mF}\cdot\text{cm}^{-2}$), Fe-CoN ($97\text{ mF}\cdot\text{cm}^{-2}$) and CoN ($72\text{ mF}\cdot\text{cm}^{-2}$), suggesting it possesses more active sites (Fig. S16). EIS (Fig. 4e and Table S4) of all samples presents that compared with CoN/CoS₂, Fe-CoN, CoN, Fe-CoS₂ and CoS₂, Fe-CoN/CoS₂ has notably low charge transfer resistance ($1.66\text{ }\Omega$), demonstrating the dopant-induced interfacial coupling enhancement can allow Fe-CoN/CoS₂ the rapid charge transfer. In addition, the stability is also a critical index of catalyst, and Fig. 4f certifies Fe-CoN/CoS₂ has outstanding stability. In Fig. S17, the 10%Fe-CoN/CoS₂, Fe-CoN/CoS₂, 20%Fe-CoN/CoS₂ at $10\text{ mA}\cdot\text{cm}^{-2}$ only display small decays of 5, 4 and 5 mV compared to the CoN/CoS₂ (12 mV), suggesting the doping of Fe can enhance the HER stability of the heterointerface. All the above results prove the dopant-induced interfacial coupling enhancement can give rise to the excellent HER performance of Fe-CoN/CoS₂ in acidic condition.

The HER performances of these catalysts were also evaluated in alkaline environment. Fig. 5a presents the LSV curves of all samples. The overpotential of Fe-CoN/CoS₂ is 72 mV at $10\text{ mA}\cdot\text{cm}^{-2}$, and it is much smaller than CoN/CoS₂ (175 mV), Fe-CoS₂ (213 mV), CoS₂ (217 mV), Fe-CoN (191 mV) and CoN (286 mV), indicating the dopant-induced interfacial coupling enhancement can obviously improve the HER performance in alkaline condition (Fig. S18 and Table S1). Fig. 5b exhibits

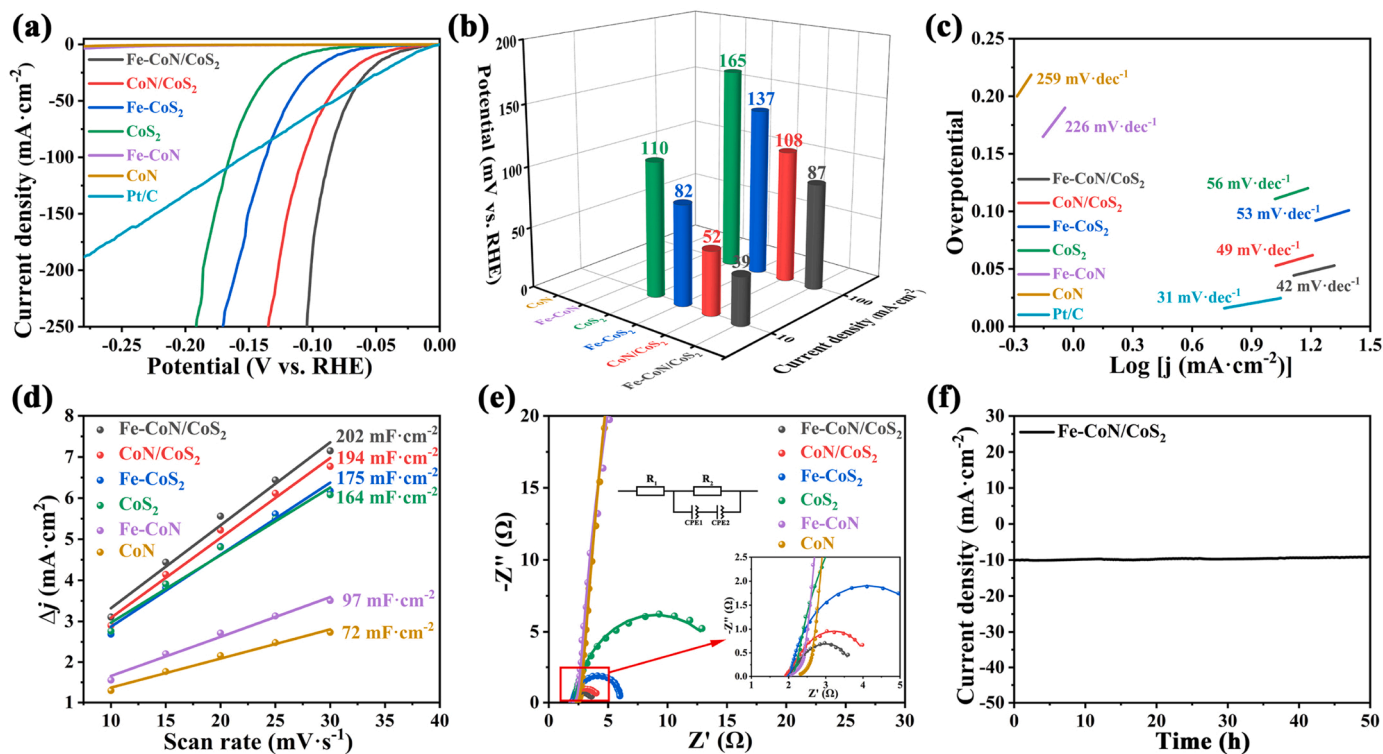


Fig. 4. In 1 M HClO₄, (a) LSV curves. (b) Corresponding overpotentials at 10 and $100\text{ mA}\cdot\text{cm}^{-2}$. (c) Tafel plots. (d) C_{dl} of the as-prepared catalysts. (e) Nyquist plots. (f) i-t curve of Fe-CoN/CoS₂ at constant potential.

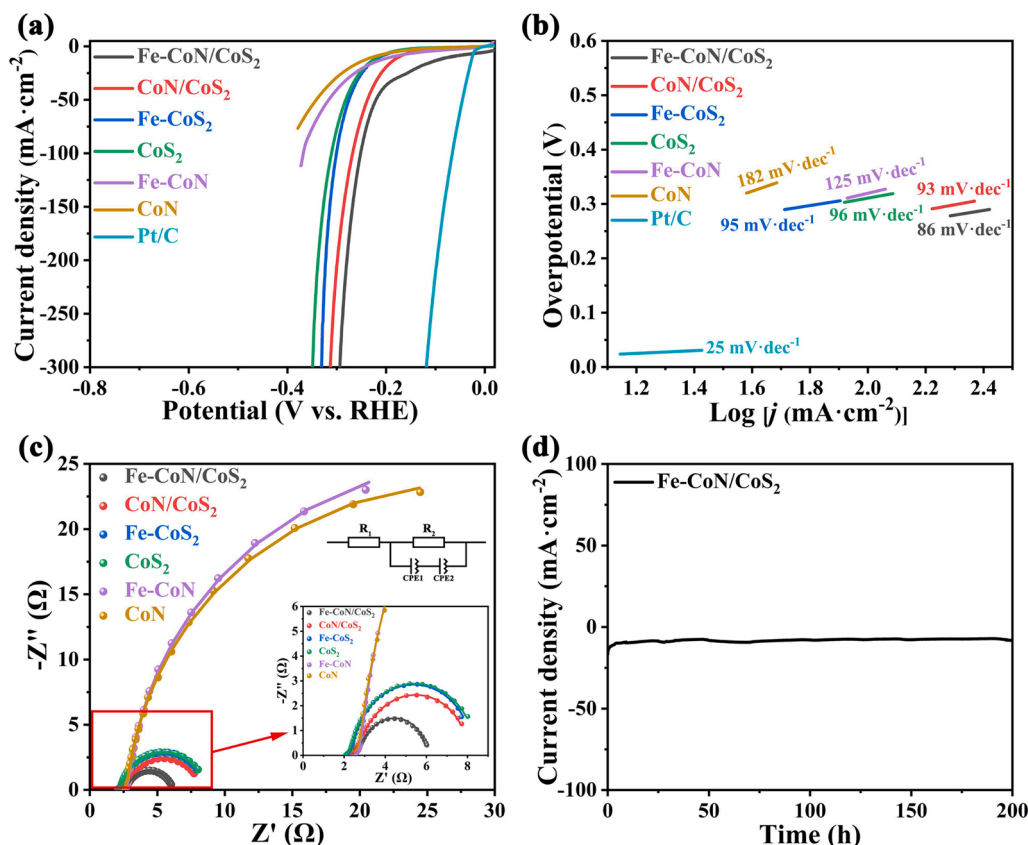


Fig. 5. In 1 M KOH, (a) LSV curves of HER. (b) Corresponding Tafel plots. (c) Nyquist plots. (d) i-t curve of Fe-CoN/CoS₂ at constant potential.

the Fe-CoN/CoS₂ is of the smallest Tafel slope (86 mV·dec⁻¹) among them, suggesting it possesses the most rapid kinetics. Fig. S19 exhibits the LSV curves of HER in alkaline condition about 20%Fe-CoN/CoS₂, Fe-CoN/CoS₂ and 10%Fe-CoN/CoS₂. The overpotential and Tafel slope of Fe-CoN/CoS₂ are also the lowest among them. Besides that, the Nyquist plots (Fig. 5c) displays that the Fe-CoN/CoS₂ has the smallest R_{ct} of 3.64 Ω , which is much less than CoN/CoS₂ (5.79 Ω), Fe-CoS₂ (6.15 Ω), CoS₂ (6.47 Ω), Fe-CoN (52.89 Ω) and CoN (54.71 Ω), implying its fast kinetics (Table S5). Moreover, an inappreciable decrease was observed after 200 h stability test, which suggests the Fe-CoN/CoS₂ has excellent HER stability in alkaline condition (Fig. 5d). Similarly, the increase of overpotential (Fig. S20) about CoN/CoS₂ (20 mV) is bigger than 10%Fe-CoN/CoS₂ (17 mV), Fe-CoN/CoS₂ (14 mV) and 20%Fe-CoN/CoS₂ (16 mV) at 10 mA·cm⁻², demonstrating the doping of Fe can enhance the stability of the heterointerface.

3.4. Overall water splitting (OWS)

Considering the above excellent HER and OER performance of the Fe-CoN/CoS₂ in alkaline condition, the OWS performances of all samples were measured in 1 M KOH. In Figs. 6a and 6b, Fe-CoN/CoS₂ needs the cell voltage of only 1.48 V to deliver the current density of 10 mA·cm⁻², much lower than CoN/CoS₂ (1.58 V), Fe-CoS₂ (1.62 V), CoS₂ (1.64 V), Fe-CoN (1.65 V), CoN (1.66 V) and RuO₂/Pt/C (1.49 V). Fig. 6c exhibits the working stability test of electrolytic cell under long time electrolysis. After 100 h testing, the current density remains 86%, whereas by contrast, the stability of RuO₂/Pt/C reduces to 61% after 35 h, indicating the Fe-CoN/CoS₂-based system is much stable than the commercial one. These achievements notably prove the Fe-CoN/CoS₂ is a nice candidate for water-splitting process with low cost, high activity and good stability.

3.5. DFT calculation analysis

The catalytic mechanism was investigated by using DFT calculations [68,69]. The theoretical model was constructed according to our TEM and XRD results, i.e. the (111) surface of CoN and (200) surface of CoS₂ were selected to construct the heterointerface of CoN/CoS₂. For Fe-CoN/CoS₂, four cobalt atoms were substituted by Fe atoms (Fe:Co = 1:7), which matches the feeding ratio. We first studied HER mechanism of all catalysts (Fig. 7a). For pristine CoN and CoS₂, the ΔG_{H^*} are 0.54 and 0.45 eV, suggesting HER activity is poor due to the strong adsorption of H^{*} on the pure CoN and CoS₂ surface. As a result of the doping with Fe, the ΔG_{H^*} drops to 0.53 and 0.42 eV, respectively, indicating the Fe-doping can weaken the adsorption of H^{*}. This proves the Fe-CoN and Fe-CoS₂ catalysts have higher HER activity than their counterparts, which is in line with the experimental results presented above. After forming the heterointerface between CoN and CoS₂, two single phase advantages can be strengthened around the interface, leading to a lower adsorption energy (0.16 eV) for CoN/CoS₂. Nevertheless, when Fe was doped into the heterointerface of CoN/CoS₂, the ΔG_{H^*} value has reduced to 0.02 eV, which is very close to zero, implying Fe-CoN/CoS₂ possesses the most appropriate hydrogen adsorption energy. Compared to other catalysts in this work, the lowest ΔG_{H^*} of Fe-CoN/CoS₂ indicates the interface coupling enhancement can further intensify the advantage of CoN/CoS₂ heterointerface, which gives rise to the most favorable adsorption kinetics for H^{*}.

Fig. 7b presents the ΔG diagram of OER, and the rate determining step (RDS) is the process from *O to *OOH for all samples, demonstrating the doping of Fe or the formation of heterointerface cannot alter the RDS of OER. However, their ΔG values of RDS are quite different. To be specific, the energy barriers of pristine CoN and CoS₂ are 2.56 and 2.05 eV, respectively, demonstrating the energy barrier to form *OOH is very high, which is not conducive to the adsorption of oxygen-

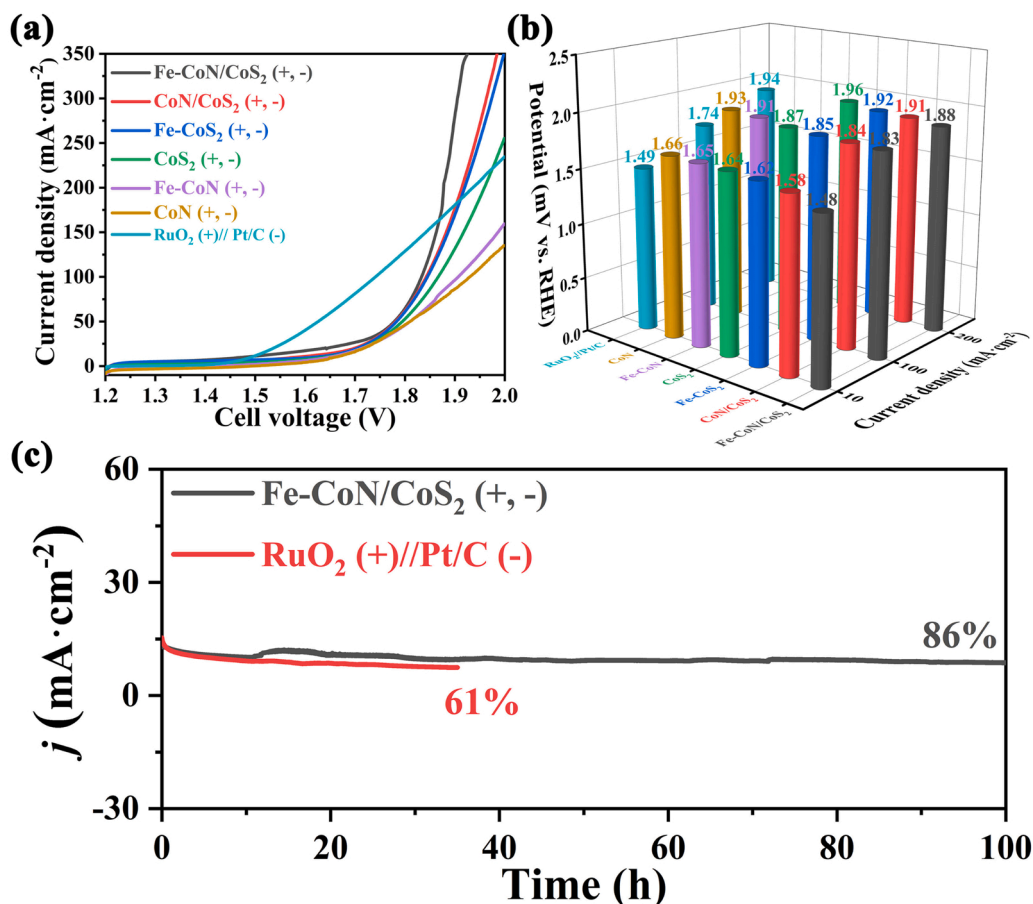


Fig. 6. In 1 M KOH, (a) Polarization curves of overall water splitting. (b) Corresponding voltages at $j = 10, 100$ and $200 \text{ mA}\cdot\text{cm}^{-2}$. (c) Long-term stability test.

containing intermediates on the active sites. After Fe-doping, the ΔG values of Fe-CoN and Fe-CoS₂ decrease to 2.46 and 2.03 eV, respectively, indicating the cooperation of Fe can decrease the energy barrier to form *OOH. When constructing the heterointerface between CoN and CoS₂, the energy barrier of CoN/CoS₂ is reduced to 1.89 eV (Fig. S21), which proves the synergistic effect from heterointerface can improve the catalytic efficiency. These results are not surprising because doping effect or the formation of heterointerface can boost electrocatalytic performance and have been previously reported [12,70]. Yet, when the heterointerface is doped by Fe, the ΔG value of Fe-CoN/CoS₂ goes straight down to 1.63 eV and the corresponding theoretical overpotential is 0.4 V (Fig. S22). The lowest ΔG_{H^*} of Fe-CoN/CoS₂ attests the interface coupling enhancement can further reinforce the advantage of CoN/CoS₂ heterointerface, resulting in the most favorable adsorption kinetics for OER. These results elucidate that the OER activity of all catalysts should be Fe-CoN/CoS₂ > CoN/CoS₂ > Fe-CoN (or Fe-CoS₂) > CoN (or CoS₂), which echoes with our experimental results.

To further get insights into electronic structure, the Bader charge and density of states (DOS) were calculated. Theoretically speaking, the charge distribution of all atoms in the original CoN/CoS₂ is relative equilibrium [71]. However, after the doping of Fe, the charge will be redistributed due to the electronegativity difference of Fe (1.83), Co (1.88), N (3.04) and S (2.58). Since the electronegativity of Co is bigger than that of Fe, the charges tend to be restricted to the Co. As shown in Fig. 7c and Fig. 7d, the charge distribution at the adsorption site changes from 8.31 to 8.34, suggesting the charge is more accumulated at the adsorption site. This charge redistribution can directly influence the interaction of heterointerface between CoN and CoS₂, leading to the interface coupling enhancement, which allows the optimal adsorption of these intermediates of HER and OER. Furthermore, in Fig. 7e, both

Fe-CoN/CoS₂ and CoN/CoS₂ display metallic characteristics owing to zero bandgap near the Fermi level. However, the intensity of PDOS at adsorption site about Fe-CoN/CoS₂ is much bigger than CoN/CoS₂ near the Fermi level, implying the conductivity of the former is better than the latter, which echoes the EIS result. All the above theoretical calculation results are in complete agreement with the experimental results.

4. Conclusions

Summarily, we have developed a novel heteroatom-doped heterogeneous interfacial catalyst (Fe-CoN/CoS₂). Consequently, Fe-CoN/CoS₂ presents superior electrocatalytic performance for HER ($\eta_{10} = 39 \text{ mV}$ in acidic condition; $\eta_{10} = 72 \text{ mV}$ in alkaline condition). Particularly, for OER, the Fe-CoN/CoS₂ exhibits an ultra-low overpotential ($\eta_{10} = 154 \text{ mV}$). Moreover, the cell voltage of OWS about Fe-CoN/CoS₂ is only 1.48 V at $10 \text{ mA}\cdot\text{cm}^{-2}$. It is found from XPS that the doping of Fe can boost the coupling of electrons at the heterogeneous interface, resulting in significantly intensive interfacial polarization, which greatly optimizes the electron distribution near the interface and significantly improves the inherent catalytic activity of the catalyst. DFT analysis unveils that the doping of Fe can modify the electronic structure around the heterointerface, resulting in a moderate adsorption of H⁺ and oxygen-containing intermediates, thus decrease the energy barriers about HER and OER and enhance the intrinsic activity. These findings provide a valid guidance for the subsequent design of transition metal ion-doping heterointerface catalysts.

CRediT authorship contribution statement

Wei Luo: Data curation, Validation, Writing – original draft. Yanli

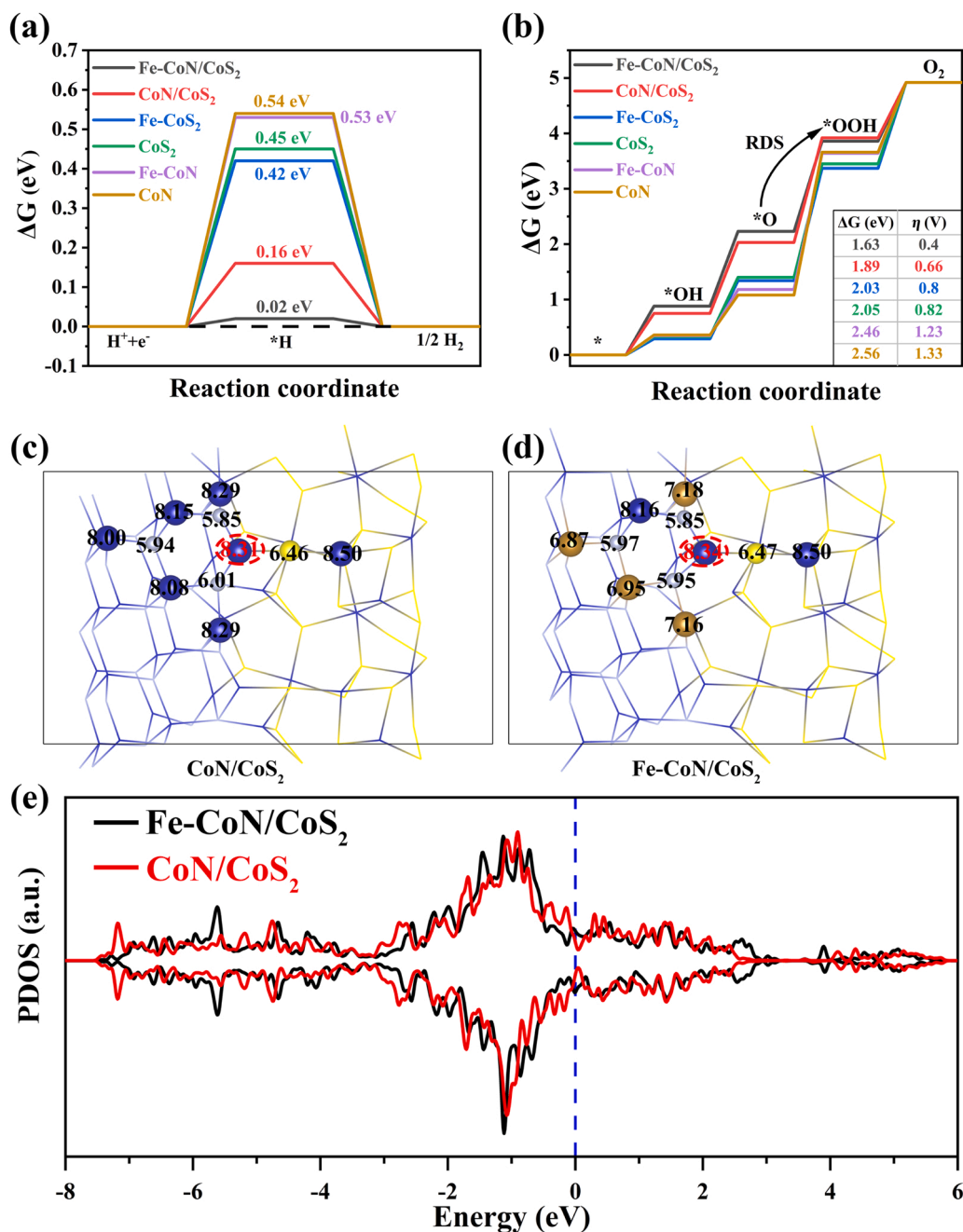


Fig. 7. The Gibbs free energy diagrams of (a) HER and (b) OER. The Bader charge numbers of atoms in (c) CoN/CoS₂ and (d) Fe-CoN/CoS₂ (Red dotted circles represent adsorption sites). (e) PDOS plot of the adsorption sites about Fe-CoN/CoS₂ and CoN/CoS₂. (The blue, white, yellow and orange balls represent Co, N, S and Fe elements, respectively.).

Yu: Data curation, Validation, Theoretical model designs and computations. **Yucheng Wu:** Data curation, Validation. **Zemian Ma:** Data curation, Validation. **Xueying Ma:** Data curation, Validation. **Yimin Jiang:** Data curation, Validation. **Wei Shen:** Theoretical model designs and computations. **Rongxing He:** Conceptualization, Funding acquisition, Supervision, Writing – review & editing. **Ming Li:** Conceptualization, Funding acquisition, Supervision, Writing – review & editing. **Wei Su:** Conceptualization, Funding acquisition, Supervision, Writing – review & editing. All authors reviewed and commented on the manuscript before publication.

Declaration of Competing Interest

The authors declare no conflict of interest.

Data Availability

Data will be made available on request.

Acknowledgements

This work was supported by the National Natural Science Foundation of China (22006120), the Innovation Research 2035 Pilot Plan of Southwest University (SWU-XDZD22011), the General Project of Chongqing Frontier and Applied Basic Research Program (cstc2020jcyj-msxmX0536) and Program for Innovation Team Building at Institutions of Higher Education in Chongqing (CXTDX201601011).

Appendix A. Supporting information

Supplementary data associated with this article can be found in the online version at [doi:10.1016/j.apcatb.2023.122928](https://doi.org/10.1016/j.apcatb.2023.122928).

References

- [1] Y. Hou, M. Qiu, M.G. Kim, P. Liu, G. Nam, T. Zhang, X. Zhuang, B. Yang, J. Cho, M. Chen, C. Yuan, L. Lei, X. Feng, Atomically dispersed nickel–nitrogen–sulfur species anchored on porous carbon nanosheets for efficient water oxidation, *Nat. Comm.* 10 (2019) 1392, <https://doi.org/10.1038/s41467-019-09394-5>.
- [2] S. Navalón, A. Dhakshinamoorthy, M. Alvaro, B. Ferrer, H. García, Metal–organic frameworks as photocatalysts for solar-driven overall water splitting, *Chem. Rev.* 123 (2022) 445–490, <https://doi.org/10.1021/acs.chemrev.2c00460>.
- [3] P. Zhou, G. Hai, G. Zhao, R. Li, X. Huang, Y. Lu, G. Wang, CeO₂ as an “electron pump” to boost the performance of Co₄N in electrocatalytic hydrogen evolution, oxygen evolution and biomass oxidation valorization, *Appl. Catal. B Environ.* 325 (2023), 122364, <https://doi.org/10.1016/j.apcatb.2023.122364>.
- [4] Y. Liu, Z. Li, H. Sun, L. Zheng, Z. Yuan, S. Li, Y. Li, X. Fang, Y. Gao, Z. Wang, X. Dai, X. Zhang, W. Song, Trace N introduction accelerates desorption of intermediates for the HER and formation of MOOH species for the OER on NiCoP to boost overall water splitting, *J. Mater. Chem. A* 11 (2023) 1256–1267, <https://doi.org/10.1039/D2TA06897D>.
- [5] M. Singh, T.T. Nguyen, M.A. P. Q.P. Ngo, D.H. Kim, N.H. Kim, J.H. Lee, Metallic metastable hybrid 1T'/1T phase triggered Co₃P-SnS₂ nanosheets for high efficiency trifunctional electrocatalyst, *Small* 19 (2023) 2206726, <https://doi.org/10.1002/smll.202206726>.
- [6] H. Su, J. Jiang, S. Song, B. An, N. Li, Y. Gao, L. Ge, Recent progress on design and applications of transition metal chalcogenide-associated electrocatalysts for the overall water splitting, *Chin. J. Catal.* 44 (2023) 7–49, [https://doi.org/10.1016/S1872-2067\(22\)64149-4](https://doi.org/10.1016/S1872-2067(22)64149-4).
- [7] T. Li, Y. Li, W. Li, S. Jia, X. Chen, X. Zhang, F. Yang, The fabrication of a flexible electrode with trace Rh based on polypyrrole for the hydrogen evolution reaction, *Chem. Comm.* 57 (2021) 7370–7373, <https://doi.org/10.1039/d1cc02004h>.
- [8] X. Wang, J. Luo, Y. Tuo, Y. Gu, W. Liu, S. Wang, Y. Zhou, J. Zhang, Hierarchical heterostructure of NiFe₂O₄ nanoflakes grown on the tip of NiCo₂O₄ nanoneedles with enhanced interfacial polarization effect to achieve highly efficient electrocatalytic oxygen evolution, *Chem. Eng. J.* 457 (2023), 141169, <https://doi.org/10.1016/j.cej.2022.141169>.
- [9] J. Liu, D. Wang, K. Huang, J. Dong, J. Liao, S. Dai, X. Tang, M. Yan, H. Gong, J. Liu, Z. Gong, R. Liu, C. Cui, G. Ye, X. Zou, H. Fei, Iodine-doping-induced electronic structure tuning of atomic cobalt for enhanced hydrogen evolution electrocatalysis, *ACS Nano* 15 (2021) 18125–18134, <https://doi.org/10.1021/acsnano.1c06796>.
- [10] P. Thangavel, H. Lee, T.-H. Kong, S. Kwon, A. Tayyebi, Immobilizing low-cost metal nitrides in electrochemically reconstructed platinum group metal (PGM)-free oxy-(hydroxides) surface for exceptional OER kinetics in anion exchange membrane water electrolysis, *Adv. Energy Mater.* 13 (2022) 2203401, <https://doi.org/10.1002/aenm.202203401>.
- [11] L. Zhang, Y. Lei, W. Xu, D. Wang, Y. Zhao, W. Chen, X. Xiang, X. Pang, B. Zhang, H. Shang, Highly active and durable nitrogen-doped CoP/CeO₂ nanowire heterostructures for overall water splitting, *Chem. Eng. J.* 460 (2023), 141119, <https://doi.org/10.1016/j.cej.2022.141119>.
- [12] L. Yan, B. Zhang, J. Zhu, Y. Li, P. Tsiakaras, P. Kang Shen, Electronic modulation of cobalt phosphide nanosheet arrays via copper doping for highly efficient neutral-pH overall water splitting, *Appl. Catal. B Environ.* 265 (2020), 118555, <https://doi.org/10.1016/j.apcatb.2019.118555>.
- [13] J.-W. Zhao, H. Zhang, C.-F. Li, X. Zhou, J.-Q. Wu, F. Zeng, J. Zhang, G.-R. Li, Key roles of surface Fe sites and Sr vacancies in the perovskite for an efficient oxygen evolution reaction via lattice oxygen oxidation, *Energy Environ. Sci.* 15 (2022) 3912–3922, <https://doi.org/10.1039/D2EE00264G>.
- [14] W. Zhang, J. Zhao, J. Zhang, X. Chen, X. Zhang, F. Yang, Electronic asymmetric distribution of RhCu bimetallic nanocrystals for enhancing trifunctional electrocatalysis, *ACS Appl. Mater. Interfaces* 12 (2020) 10299–10306, <https://doi.org/10.1021/acsami.9b19980>.
- [15] X. Zhou, Y. Mo, F. Yu, L. Liao, X. Yong, F. Zhang, D. Li, Q. Zhou, T. Sheng, H. Zhou, Engineering active iron sites on nanoporous bimetal phosphide/nitride heterostructure array enabling robust overall water splitting, *Adv. Funct. Mater.* 33 (2023) 2209465, <https://doi.org/10.1002/adfm.202209465>.
- [16] W. Zhang, N. Han, J. Luo, X. Han, S. Feng, W. Guo, S. Xie, Z. Zhou, P. Subramanian, K. Wan, J. Arbiol, C. Zhang, S. Liu, M. Xu, X. Zhang, J. Fransaer, Critical role of phosphorus in hollow structures cobalt-based phosphides as bifunctional catalysts for water splitting, *Small* 18 (2022) 2103561, <https://doi.org/10.1002/smll.202103561>.
- [17] R. Andaveh, A. Sabour Rouhaghdam, J. Ai, M. Maleki, K. Wang, A. Seif, G. Barati Darband, J. Li, Boosting the electrocatalytic activity of NiSe by introducing MnCo as an efficient heterostructured electrocatalyst for large-current-density alkaline seawater splitting, *Appl. Catal. B Environ.* 325 (2023), 122355, <https://doi.org/10.1016/j.apcatb.2022.122355>.
- [18] J. Zhang, J. Dang, X. Zhu, J. Ma, M. Ouyang, F. Yang, Ultra-low Pt-loaded catalyst based on nickel mesh for boosting alkaline water electrolysis, *Appl. Catal. B Environ.* 325 (2023), 122296, <https://doi.org/10.1016/j.apcatb.2022.122296>.
- [19] J.W. Zhao, C.F. Li, Z.X. Shi, J.L. Guan, G.R. Li, Boosting lattice oxygen oxidation of perovskite to efficiently catalyze oxygen evolution reaction by FeOOH decoration, *Research* 2020 (2020) 6961578, <https://doi.org/10.34133/2020/6961578>.
- [20] L. Zhong, L. He, N. Wang, Y. Chen, X. Xie, B. Sun, J. Qian, S. Komarneni, W. Hu, Preparation of metal-organic framework from in situ self-sacrificial stainless-steel matrix for efficient water oxidation, *Appl. Catal. B Environ.* 325 (2023), 122343, <https://doi.org/10.1016/j.apcatb.2022.122343>.
- [21] Q. Wang, Y. Cheng, H.B. Tao, Y. Liu, X. Ma, D.-S. Li, H.B. Yang, B. Liu, Long-term stability challenges and opportunities in acidic oxygen evolution electrocatalysis, *Angew. Chem. Int. Ed.* 62 (2023), e202216645, <https://doi.org/10.1002/anie.202216645>.
- [22] A. Shahzad, F. Zulfiqar, M. Arif Nadeem, Cobalt containing bimetallic ZIFs and their derivatives as OER electrocatalysts: a critical review, *Coord. Chem. Rev.* 477 (2023), 214925, <https://doi.org/10.1016/j.ccr.2022.214925>.
- [23] Y. Li, L. Ji, X. Zhou, T. Li, X. Chen, X. Zhang, F. Yang, Co–Mo–S nanoflowers wrapped oxidized multi-walled carbon nanotubes as efficient electrocatalysts for oxygen evolution reaction, *ChemCatChem* 13 (2021) 3270–3274, <https://doi.org/10.1002/cctc.202100432>.
- [24] X. Chen, W. Liao, M. Zhong, J. Chen, S. Yan, W. Li, C. Wang, W. Chen, X. Lu, Rational design of robust iridium-ceria oxide-carbon nanofibers to boost oxygen evolution reaction in both alkaline and acidic media, *Nano Res* (2022), <https://doi.org/10.1007/s12274-022-5280-8>.
- [25] C. Wang, M. Humayun, D.P. Debecker, Y. Wu, Electrocatalytic water oxidation with layered double hydroxides confining single atoms, *Coord. Chem. Rev.* 478 (2023), 214973, <https://doi.org/10.1016/j.ccr.2022.214973>.
- [26] C.F. Li, L.J. Xie, J.W. Zhao, L.F. Gu, H.B. Tang, L. Zheng, G.R. Li, Interfacial Fe–O–Ni–O–Fe bonding regulates the active Ni sites of Ni-MOFs via iron doping and decorating with FeOOH for super-efficient oxygen evolution, *Angew. Chem. Int. Ed. Engl.* 61 (2022), e202116934, <https://doi.org/10.1002/anie.202116934>.
- [27] M. Fei, H. Shi, J. Zhao, N. Kang, W. He, H. Li, F. Yang, Porous microspherical N and P-co-doped NiFe₂O₄/single-walled carbon nanotubes for efficient electrochemical oxygen evolution reaction, *ChemCatChem* 10 (2018) 5174–5181, <https://doi.org/10.1002/cctc.201801019>.
- [28] L. Gao, X. Zhong, J. Chen, Y. Zhang, J. Liu, B. Zhang, Optimizing the electronic structure of Fe-doped Co₃O₄ supported Ru catalyst via metal-support interaction boosting oxygen evolution reaction and hydrogen evolution reaction, *Chin. Chem. Lett.* (2022), 108085, <https://doi.org/10.1016/j.ccl.2022.108085>.
- [29] R. Zhang, L. Zhu, W. Lv, M. Wei, L. Wang, W. Wang, Facile synthesis of Ni₃S₂ nanosheets with abundant active sites induced by Fe incorporation on Ni foam for enhanced oxygen evolution reaction, *Appl. Surf. Sci.* 610 (2023), 155537, <https://doi.org/10.1016/j.apsusc.2022.155537>.
- [30] Y. Zhu, X. Wang, X. Zhu, Z. Wu, D. Zhao, F. Wang, D. Sun, Y. Tang, H. Li, G. Fu, Improving the oxygen evolution activity of layered double-hydroxide via erbium-induced electronic engineering, *Small* 19 (2023) 2206531, <https://doi.org/10.1002/smll.202206531>.
- [31] J. Qiao, Z. Bao, L. Kong, X. Liu, C. Lu, M. Ni, W. He, M. Zhou, Z. Sun, MOF-derived heterostructure CoNi/CoNiP anchored on MXene framework as a superior bifunctional electrocatalyst for zinc-air batteries, *Chin. Chem. Lett.* (2023), 108318, <https://doi.org/10.1016/j.ccl.2023.108318>.
- [32] Y. Gao, L. Bai, X. Zhang, F. Yang, Non-parallel photo-assisted electrocatalysis mechanism of SnS₂/NiO heterojunction for efficient electrocatalytic oxygen evolution reaction, *ChemElectroChem* 8 (2021) 2087–2093, <https://doi.org/10.1002/celec.202100464>.
- [33] W. Chen, X. Zhu, R. Wang, W. Wei, M. Liu, S. Dong, K.K. Ostrikov, S.-Q. Zang, Interface-engineered MoS₂/CoS/NF bifunctional catalysts for highly-efficient water electrolysis, *J. Energy Chem.* 75 (2022) 16–25, <https://doi.org/10.1016/j.jechem.2022.08.012>.
- [34] C.X. Zhao, J.N. Liu, J. Wang, D. Ren, B.Q. Li, Q. Zhang, Recent advances of noble-metal-free bifunctional oxygen reduction and evolution electrocatalysts, *Chem. Soc. Rev.* 50 (2021) 7745–7778, <https://doi.org/10.1039/d1cs00135c>.
- [35] Z. Li, M. Hu, P. Wang, J. Liu, J. Yao, C. Li, Heterojunction catalyst in electrocatalytic water splitting, *Coord. Chem. Rev.* 439 (2021), 213953, <https://doi.org/10.1016/j.ccr.2021.213953>.
- [36] J. Wang, M. Zhang, G. Yang, W. Song, W. Zhong, X. Wang, M. Wang, T. Sun, Y. Tang, Heterogeneous bimetallic Mo-NiP₂/Ni₃S₂ as a highly efficient electrocatalyst for robust overall water splitting, *Adv. Funct. Mater.* 31 (2021) 2101532, <https://doi.org/10.1002/adfm.202101532>.
- [37] D. Kim, Z. Zhang, K. Yong, Synergistic doping effects of a ZnO:N/BiVO₄:Mo bunched nanorod array photoanode for enhancing charge transfer and carrier density in photoelectrochemical systems, *Nanoscale* 10 (2018) 20256–20265, <https://doi.org/10.1039/C8NR06630B>.
- [38] I. Ledezma-Yanez, W.D.Z. Wallace, P. Sebastián-Pascual, V. Climent, J.M. Feliu, M. T.M. Koper, Interfacial water reorganization as a pH-dependent descriptor of the hydrogen evolution rate on platinum electrodes, *Nat. Energy* 2 (2017) 17031, <https://doi.org/10.1038/nenergy.2017.31>.
- [39] C.-F. Li, L.-J. Xie, J.-W. Zhao, L.-F. Gu, J.-Q. Wu, G.-R. Li, Interfacial electronic modulation by Fe₂O₃/NiFe-LDHs heterostructures for efficient oxygen evolution at high current density, *Appl. Catal. B Environ.* 306 (2022), 121097, <https://doi.org/10.1016/j.apcatb.2022.121097>.
- [40] L. Zeng, K. Sun, X. Wang, Y. Liu, Y. Pan, Z. Liu, D. Cao, Y. Song, S. Liu, C. Liu, Three-dimensional networked Ni₂P/Ni₃S₂ heteronanoarrays for highly enhanced electrochemical overall-water-splitting activity, *Nano Energy* 51 (2018) 26–36, <https://doi.org/10.1016/j.nanoen.2018.06.048>.
- [41] H. Zhang, B. Xi, Y. Gu, W. Chen, S. Xiong, Interface engineering and heterometal doping Mo-NiS/Ni(OH)₂ for overall water splitting, *Nano Res* 14 (2021) 3466–3473, <https://doi.org/10.1007/s12274-021-3557-y>.
- [42] N. Cao, S. Chen, Y. Di, C. Li, H. Qi, Q. Shao, W. Zhao, Y. Qin, X. Zang, High efficiency in overall water-splitting via Co-doping heterointerface-rich NiS₂/MoS₂

- nanosheets electrocatalysts, *Electrochim. Acta* 425 (2022), 140674, <https://doi.org/10.1016/j.electacta.2022.140674>.
- [43] H. Su, S. Song, S. Li, Y. Gao, L. Ge, W. Song, T. Ma, J. Liu, High-valent bimetal $\text{Ni}_3\text{S}_2/\text{Co}_3\text{S}_4$ induced by Cu doping for bifunctional electrocatalytic water splitting, *Appl. Catal. B Environ.* 293 (2021), 120225, <https://doi.org/10.1016/j.apcatb.2021.120225>.
- [44] Y.-J. Tang, Y. Zou, D. Zhu, Efficient water oxidation using an Fe-doped nickel telluride-nickel phosphide electrocatalyst by partial phosphating, *J. Mater. Chem. A* 10 (2022) 12438–12446, <https://doi.org/10.1039/d2ta02620a>.
- [45] P. Hohenberg, W. Kohn, Inhomogeneous electron gas, *Phys. Rev.* 136 (1964) B864–B871, <https://doi.org/10.1103/PhysRev.136.B864>.
- [46] W. Kohn, L.J. Sham, Self-consistent equations including exchange and correlation effects, *Phys. Rev.* 140 (1965) A1133–A1138, <https://doi.org/10.1103/PhysRev.140.A1133>.
- [47] G. Kresse, J. Hafner, Ab initio molecular dynamics for liquid metals, *Phys. Rev. B Condens. Matter* 47 (1993) 558–561, <https://doi.org/10.1103/physrevb.47.558>.
- [48] P.E. Blochl, Projector augmented-wave method, *Phys. Rev. B Condens. Matter* 50 (1994) 17953–17979, <https://doi.org/10.1103/physrevb.50.17953>.
- [49] S. Hunsche, T. Starczewski, A. l'Huillier, A. Persson, C.G. Wahlström, H.B. van Linden van den Heuvell, S. Svanberg, Ionization and fragmentation of C_{60} via multiphoton-multiphoton excitation, *Phys. Rev. Lett.* 77 (10) (1996) 1966–1969, <https://doi.org/10.1103/PhysRevLett.77.1966>.
- [50] G. Kresse, J. Furthmüller, Efficient iterative schemes for ab initio total-energy calculations using a plane-wave basis set, *Phys. Rev. B* 54 (1996) 11169–11186, <https://doi.org/10.1103/PhysRevB.54.11169>.
- [51] H.J. Monkhorst, J.D. Pack, Special points for brillouin-zone integrations, *Phys. Rev. B* 13 (1976) 5188–5192, <https://doi.org/10.1103/PhysRevB.13.5188>.
- [52] C.-F. Li, T.-Y. Shuai, L.-R. Zheng, H.-B. Tang, J.-W. Zhao, G.-R. Li, The key role of carboxylate ligands in Ru@Ni-MOFs/NF in promoting water dissociation kinetics for effective hydrogen evolution in alkaline media, *Chem. Eng. J.* 451 (2023), 138618, <https://doi.org/10.1016/j.cej.2022.138618>.
- [53] P. Ji, R. Yu, P. Wang, X. Pan, H. Jin, D. Zheng, D. Chen, J. Zhu, Z. Pu, J. Wu, S. Mu, Ultra-Fast and In-depth reconstruction of transition metal fluorides in electrocatalytic hydrogen evolution processes, *Adv. Sci.* 9 (2022) 2103567, <https://doi.org/10.1002/advs.202103567>.
- [54] I. Barlocco, L.A. Cipriano, G. Di Liberto, G. Pacchioni, Does the oxygen evolution reaction follow the classical OH^* , O^* , OOH^* path on single atom catalysts? *J. Catal.* 417 (2023) 351–359, <https://doi.org/10.1016/j.jcat.2022.12.014>.
- [55] M. Guo, R. Deng, C. Wang, Q. Zhang, Recent progress of advanced manganese oxide-based materials for acidic oxygen evolution reaction: fundamentals, performance optimization, and prospects, *J. Energy Chem.* 78 (2023) 537–553, <https://doi.org/10.1016/j.jechem.2022.11.054>.
- [56] M. García-Mota, M. Bajdich, V. Viswanathan, A. Vojvodic, A.T. Bell, J.K. Nørskov, Importance of correlation in determining electrocatalytic oxygen evolution activity on cobalt oxides, *J. Phys. Chem. C* 116 (2012) 21077–21082, <https://doi.org/10.1021/jp306303y>.
- [57] Y. Sun, T. Zhang, X. Li, D. Liu, G. Liu, X. Zhang, X. Lyu, W. Cai, Y. Li, Mn doped porous cobalt nitride nanowires with high activity for water oxidation under both alkaline and neutral conditions, *Chem. Commun.* 53 (2017) 13237–13240, <https://doi.org/10.1039/c7cc07962a>.
- [58] F. Liu, W. He, Y. Li, F. Wang, J. Zhang, X. Xu, Y. Xue, C. Tang, H. Liu, J. Zhang, Activating sulfur sites of CoS_2 electrocatalysts through tin doping for hydrogen evolution reaction, *Appl. Surf. Sci.* 546 (2021), 149101, <https://doi.org/10.1016/j.apsusc.2021.149101>.
- [59] X. Luo, P. Ji, P. Wang, R. Cheng, D. Chen, C. Lin, J. Zhang, J. He, Z. Shi, N. Li, S. Xiao, S. Mu, Interface engineering of hierarchical branched Mo-doped $\text{Ni}_3\text{S}_2/\text{Ni}_x\text{P}_y$ hollow heterostructure nanorods for efficient overall water splitting, *Adv. Energy Mater.* 10 (2020) 1903891, <https://doi.org/10.1002/aenm.201903891>.
- [60] Z. Xia, B. Deng, Y. Wang, Z. Jiang, Z.-J. Jiang, Synergistic co-doping induced high catalytic activities of La/Fe doped Co_3O_4 towards oxygen reduction/evolution reactions for Zn-air, Batter., *J. Mater. Chem. A* 10 (2022) 23483–23493, <https://doi.org/10.1039/d2ta06726a>.
- [61] Y. He, X. Liu, G. Chen, J. Pan, A. Yan, A. Li, X. Lu, D. Tang, N. Zhang, T. Qiu, R. Ma, T. Sasaki, Synthesis of Co(II)-Fe(III) hydroxide nanocones with mixed octahedral/tetrahedral coordination toward efficient electrocatalysis, *Chem. Mater.* 32 (2020) 4232–4240, <https://doi.org/10.1021/acs.chemmater.0c00512>.
- [62] Y. Wang, D. Liu, Z. Liu, C. Xie, J. Huo, S. Wang, Porous cobalt-iron nitride nanowires as excellent bifunctional electrocatalysts for overall water splitting, *Chem. Commun.* 52 (2016) 12614–12617, <https://doi.org/10.1039/c6cc06608a>.
- [63] B. Zhang, J. Shan, W. Wang, P. Tsiakaras, Y. Li, Oxygen vacancy and core-shell heterojunction engineering of anemone-like $\text{CoP}@\text{CoOOH}$ bifunctional electrocatalyst for efficient overall water splitting, *Small* 18 (2022), e2106012, <https://doi.org/10.1002/sml.202106012>.
- [64] J. Tang, Q. Ruan, H. Yu, C. Huang, Activating $\text{Co}(\text{OH})_2$ active sites by coupled with V_2O_5 to boost highly efficient oxygen evolution reaction, *Adv. Sustain. Syst.* (2023) 2200473, <https://doi.org/10.1002/advs.202200473>.
- [65] Y. Zhang, H. Guo, P. Yuan, K. Pang, B. Cao, X. Wu, L. Zheng, R. Song, Structural evolution of CoMoO_4 to CoOOH by ion electrochemical etching for boosting oxygen evolution reaction, *J. Power Sources* 442 (2019), 227252, <https://doi.org/10.1016/j.jpowsour.2019.227252>.
- [66] X. Zhao, Q. Han, J. Li, X. Du, G. Liu, Y. Wang, L. Wu, Z. Chen, Ordered macroporous design of sacrificial Co/VN nano-heterojunction as bifunctional oxygen electrocatalyst for rechargeable zinc-air batteries, *Chem. Eng. J.* 433 (2022), 133509, <https://doi.org/10.1016/j.cej.2021.133509>.
- [67] S. Wei, X. Wang, J. Wang, X. Sun, L. Cui, W. Yang, Y. Zheng, J. Liu, CoS_2 nanoneedle array on Ti mesh: A stable and efficient bifunctional electrocatalyst for urea-assisted electrolytic hydrogen production, *Electrochim. Acta* 246 (2017) 776–782, <https://doi.org/10.1016/j.electacta.2017.06.068>.
- [68] C. Huang, Y. Zhang, X. Li, H. Cao, Y. Guo, C. Zhang, Mn-incorporated Co_3O_4 bifunctional electrocatalysts for zinc-air battery application: An experimental and DFT study, *Appl. Catal. B Environ.* 319 (2022), 121909, <https://doi.org/10.1016/j.apcatb.2022.121909>.
- [69] D. Tian, S.R. Denny, K. Li, H. Wang, S. Kattel, J.G. Chen, Density functional theory studies of transition metal carbides and nitrides as electrocatalysts, *Chem. Soc. Rev.* 50 (2021) 12338–12376, <https://doi.org/10.1039/d1cs00590a>.
- [70] L. Tan, J. Yu, H. Wang, H. Gao, X. Liu, L. Wang, X. She, T. Zhan, Controllable synthesis and phase-dependent catalytic performance of dual-phase nickel selenides on Ni foam for overall water splitting, *Appl. Catal. B Environ.* 303 (2022), 120915, <https://doi.org/10.1016/j.apcatb.2021.120915>.
- [71] H. Su, S. Song, Y. Gao, N. Li, Y. Fu, L. Ge, W. Song, J. Liu, T. Ma, In situ electronic redistribution tuning of NiCo_2S_4 nanosheets for enhanced electrocatalysis, *Adv. Funct. Mater.* 32 (2022) 2109731, <https://doi.org/10.1002/adfm.202109731>.